

Fabry-Pérot observations of the HH 110 jet

A. Riera ^{1,2,3}

Departament de Física i Enginyeria Nuclear, Universitat Politècnica de Catalunya, Av. Víctor Balaguers/n E-08800 Vilanova i La Geltrú, Spain

Departament d'Astronomia i Meteorologia, Universitat de Barcelona, Av. Diagonal 647, E-08028 Barcelona, Spain

On sabbatical leave at the Instituto de Ciencias Nucleares, UNAM

`angels.riera@upc.es, ariera@nuclecu.unam.mx`

A. C. Raga ³

Instituto de Ciencias Nucleares, UNAM, Ap. 70-543, 04510 D.F., México

`raga@astroscu.unam.mx`

B. Reipurth ⁴

Institute for Astronomy, University of Hawaii, 2680 Woodlawn Drive, Honolulu, HI 96822, USA

`reipurth@ifh.hawaii.edu`

Ph. Amram, J. Boulesteix ⁵

Laboratoire d'Astrophysique de Marseille, 2 Place Le Verrier, 13248 Marseille, France

`philippe.amram@oamp.fr, jacques.boulesteix@oamp.fr`

J. Cantó, O. Toledano ⁶

Instituto de Astronomia, UNAM, Ap. 70-264, 04510 D.F., México

ABSTRACT

We have obtained a $H\alpha$ position-velocity cube from Fabry-Pérot interferometric observations of the HH 110 flow. We analyze the results in terms of anisotropic wavelet transforms, from which we derive the spatial distribution of the knots as well as their characteristic sizes (along and across the outflow axis). We then study the spatial behaviour of the line width and the central radial

velocity. The results are interpreted in terms of a simple “mean flow+turbulent eddy” jet/wake model. We find that most of the observed kinematics appear to be a direct result of the mean flow, on which are superposed low amplitude ($\sim 35 \text{ km s}^{-1}$) turbulent velocities.

Subject headings: ISM: Herbig-Haro objects – ISM: jets and outflows – ISM: kinematics and dynamics – ISM: individual (HH 110)

1. Introduction

The HH 110 Herbig-Haro jet was discovered by Reipurth & Olberg (1991), and it presents a complex structure of aligned knots, which opens out with an unusually large angle of $\sim 10^\circ$. While HH objects such as HH 34 or HH 111 show aligned knots with more or less organized, arc-like shapes, HH 110 has a more chaotic structure, more reminiscent of a turbulent flow.

A possible explanation for the fact that HH 110 is different from other HH jets has been proposed by Reipurth, Raga & Heathcote (1996), who suggested that HH 110 is the result of a deflection of the adjacent HH 270 jet (which travels approximately in an E-W direction) through a collision with a dense molecular cloud core. This interpretation was supported by the fact that while the source of the HH 270 jet is detected in the radio free-free continuum, no such source is detected along the HH 110 axis (Rodríguez et al. 1998). Also, infrared images show H_2 emission concentrated on the W side of the HH 110 jet (Davis, Mundt & Eisloffel 1994; Noriega-Crespo et al. 1996), which would correspond to the region in which the jet is in contact with the dense cloud which produces the deflection. Against the jet/cloud collision scenario are the results of Choi (2001), who do not find molecular (HCO^+) emission around the jet/cloud impact point, as might be expected.

There are a series of papers which describe analytic and numerical models meant specifically for HH 110 as a jet/cloud impact flow (Raga & Cantó 1995; de Gouveia dal Pino 1999; Hurka, Schmid-Burgk & Hardee 1999). The latest models of this object are the ones of Raga et al. (2002), who have carried out the most detailed simulations up to now of this object, and computed $\text{H}\alpha$ and molecular hydrogen emission maps which agree with the observations in a qualitatively successful way. These authors also suggest that the point at which the HH 270 jet is currently impacting the cloud might have moved westwards of the HH 110 axis (i. e., deeper into the cloud), which would explain the lack of HCO^+ emission in the crossing region of the HH 270 and HH 110 axes.

In a recent paper, Riera et al. (2003) have discussed the kinematics and excitation along

and across the HH 110 outflow, as derived from long-slit spectra obtained with 5 slit positions (one along and four across the outflow axis), finding very complex structures. In the present paper, we discuss new Fabry-Pérot data which cover only the H α line, but give a full spatial coverage of the well resolved HH 110 outflow. The full spatial coverage of the position-velocity cube obtained from our data allows us to carry out a somewhat novel analysis (at least, in the context of HH objects). As the observed spatial and kinematical structures are very chaotic, and appear to defy a direct description, we have chosen to describe these structures through a wavelet analysis. A wavelet transform of an image gives information similar to the one that could be obtained from a more standard Fourier analysis, but also preserves the spatial information.

In this way one can obtain, for example, the characteristic sizes (along and across the outflow axis) of the knots as a function of position along the jet. This kind of information could also be retrieved by carrying out fits to the intensity profiles of the knots (e. g., with anisotropic Gaussian functions, as has been done in the past for other objects by Raga, Mundt & Ray 1991), but such an approach is impractical for an object as complex as HH 110, in which knots of different shapes coexist across the sections of the outflow.

We therefore obtain a position-velocity cube from our Fabry-Pérot observations (described in §2), and obtain velocity channel maps from which we compute an H α image, as well as radial velocity and line width maps (see §3). We then carry out an anisotropic wavelet analysis of the H α image, and determine the spatial scales present in the map as a function of position along the outflow (§4). We then study the variations of the line width and the radial velocity of the emission as a function of spatial scale and of position along and across the jet (§5). Finally, we interpret this kinematic information in terms of a “mean flow+turbulent eddy” model of a turbulent jet (or wake), and use the model to deduce the mean flow parameters that are relevant for the HH 110 jet (§6). The results are then summarized in §7.

2. Observations

The observations were obtained at the European Southern Observatory 3.6m telescope in January 1997. The Fabry-Pérot instrument CIGALE ¹ was used. It is composed of a focal reducer (bringing the original f/8 focal ratio of the Cassegrain focus to f/2), a scanning Fabry-Pérot and an Image Photon Counting System (IPCS). Table 1 contains the journal of

¹The instrument CIGALE (for Cinématique des GALaxieEs) is a visiting instrument belonging to the Laboratoire d’Astrophysique de Marseille.

the observations. We have used a Fabry-Pérot with an interference order $p = 793$ (380 km s^{-1}) and a *Finesse* $F = 11$. The IPCS, with a time sampling of $1/50$ second and zero readout noise, makes it possible to scan the interferometer rapidly, avoiding sky transparency, air-mass and seeing variation problems during the exposures and thus has several advantages over a CCD for this application. The exposure time per elementary channel was 5 seconds. Several observations of HH 110 have been obtained in $\text{H}\alpha$ during 2 nights. The two sets of observations in the $\text{H}\alpha$ line have been done using 2 different interference filters in order to check if the shape of the interference filter affects the shape of the $\text{H}\alpha$ profiles. A 18300 s exposure was obtained with a $\lambda_0 = 6563 \text{ \AA}$ (central wavelength) and $\Delta\lambda = 9 \text{ \AA}$ (FWHM of transmission function) filter, and a 3600 s exposure was obtained with a $\lambda_0 = 6564 \text{ \AA}$ and $\Delta\lambda = 17 \text{ \AA}$ filter.

The reduction of the data cubes was performed using the CIGALE software. The data reduction procedure has been extensively described in Amram et al. (1992, 1993, 1994, 1995, 1996, 1998). Wavelength calibration was obtained by scanning the narrow Ne 6599 \AA line under the same conditions as the observations. Velocities measured relative to the systemic velocity are very accurate, with an error of a fraction of a channel width ($< 3 \text{ km s}^{-1}$) over the whole field.

The signal measured along the scanning sequence was separated into two parts: (1) an almost constant level produced by the continuum light in a narrow passband around the line and (2) a varying part produced by the line. The continuum level was taken to be the mean of the three faintest channels, to avoid channel noise effects. The integrated line flux map was obtained by integrating the monochromatic profile in each pixel. The velocity sampling was 16 km s^{-1} . Strong OH night sky lines passing through the filters were subtracted by determining the level of emission from extended regions away from the HH object (Laval et al. 1987).

3. The $\text{H}\alpha$ channel maps, radial velocities and line widths

Figure 1 shows the velocity channel maps obtained from the Fabry-Pérot data of HH 110. We detect $\text{H}\alpha$ emission in heliocentric radial velocities ranging from -100 to $+80 \text{ km s}^{-1}$, with peak intensities in the -38.3 and -22.5 km s^{-1} channel maps.

From the line profiles at each position, we have computed the velocity of the emission peak (with a parabolic fit) and the FWHM (with linear fits to the sides of the line profiles), as well as the line flux (by adding the fluxes of the individual channels). The results are shown in Figure 2.

The integrated $H\alpha$ map obtained from the present data looks similar to previously published $H\alpha$ images of this object, showing a complex structure of knots that broadens out to the South. The radial velocities have low values ($\sim 0 \rightarrow -60 \text{ km s}^{-1}$), with more negative values to the South (see Fig. 2). The radial velocity structure across the jet is complex, showing variabilities which do not appear to show systematic trends. These results are qualitatively consistent with the radial velocities of this flow which have been previously obtained from long-slit spectroscopy (Reipurth et al. 1996; Riera et al. 2003). The FWHM of the $H\alpha$ line ranges from 50 to 100 km s^{-1} , and also shows a complex spatial structure (see Fig. 2).

Because of the complexity of the observed structures, we have carried out an analysis based on wavelet transforms, which allows us to obtain a general description of the flow without attempting a somewhat hopeless “knot by knot” description of the observations.

4. Wavelet analysis of the $H\alpha$ image

4.1. The anisotropic wavelet transforms

Wavelet transforms have been used in different astrophysical contexts. For example, Gill & Henriksen (1990) have used wavelet transforms to describe the complex structures observed in CO radial velocities of molecular clouds. Obtaining a description of the complex structure of the HH 110 jet belongs to the same class of problem, i.e., identifying the characteristics of complex spatial structures without losing the positional information. Therefore, we have applied a wavelet transform analysis to our Fabry-Pérot data.

A 2D wavelet transform analysis of the $H\alpha$ image of HH 110 can be used to obtain the positions of all of the “knots”, as well as their characteristic sizes. This kind of procedure is described, e. g., in the book of Holschneider (1995).

Once we have obtained the positions and the characteristic sizes of the $H\alpha$ structures of the HH 110 jet from the wavelet spectrum, we calculate the spatial averages of the deviations of the line center velocity and of the line widths (averaging over the characteristic sizes of the structures) in order to study the turbulence in the HH 110 jet (see §5). This procedure is completely equivalent to the one followed by Gill & Henriksen (1990).

An interesting difference between our case and the “turbulent molecular cloud” study of Gill & Henriksen (1990) is that a jet flow has two clearly defined directions : along and across the flow axis. Because of this, it is reasonable to expect that the characteristics of the structures along and across the flow axis might differ. To allow for this effect, we first

rotate the H α image so that the flow axis is parallel to the ordinate. On this rotated image, we then carry out a decomposition in a basis of anisotropic wavelets, which have different sizes along and across the outflow axis.

In particular, we have used a basis of “Mexican hat” wavelets of the form

$$g(r) = C(2 - r^2)e^{-r^2/2}, \quad (1)$$

where $r = [(x/a_x)^2 + (y/a_y)^2]^{1/2}$, and a_x and a_y are the scale lengths of the wavelet along the x - and y -axes, respectively. After trying several different possibilities, we have chosen a $C = (a_x^2 + a_y^2)^{-1/2}$ normalization. It is possible to use other normalizations (e. g., $C = \sqrt{a_x a_y}$), which lead to slightly different results, as the power is rearranged over different regions of the wavelet spectrum. However, the positions of the different peaks of the wavelet spectrum (see below) are not strongly affected by the choice of normalization.

The process that is carried out in order to compute the wavelet transform is to choose a range for a_x and a_y (which are taken to have integer values of pixels). For all of the possible (a_x, a_y) pairs we then compute the convolutions

$$T_{a_x, a_y}(x, y) = \int \int I(x', y') g(r') dx' dy', \quad (2)$$

where $r' = \{[(x' - x)/a_x]^2 + [(y' - y)/a_y]^2\}^{1/2}$, and $I(x, y)$ is the observed map as a function of the pixel position (x, y) . These convolutions are calculated with a standard FFT algorithm.

With this process, we then produce the transform maps $T_{a_x, a_y}(x, y)$, corresponding to versions of the observed map $I(x, y)$ which have been smoothed with the different g_{a_x, a_y} wavelets. These maps can be used as follows.

We first fix a position y along the observed jet. Keeping this value of y fixed, we find the finite set of values $(x_k, a_{x,k}, a_{y,k})$ corresponding to the position across the jet and the spatial scales (across and along the jet) at which the wavelet transform has local maxima in the a_x and a_y dimensions as well as in either the x or in the y dimensions. In this way, for each y we detect the positions x_k of the knots (which correspond to intensity maxima either along or across the jet axis), as well as their characteristic sizes ($a_{x,k}$ and $a_{y,k}$). In practice, at many positions y along the jet one finds a single maximum, but in some positions up to three maxima are found, corresponding to different structures observed across the HH 110 jet.

4.2. The H α “image”

The results obtained with the process described in §4.1 are shown in Figure 3. This figure shows the H α image (see §3), which we have rotated by 13° so that the outflow is more or less parallel to the y -axis. We have then convolved this map with a set of wavelets with $1 \leq a_x \leq 20$ pixels (with 0".91 per pixel) and $1 \leq a_y \leq 20$ pixels. The values of the peaks x_k of the wavelet transform obtained for each position y along the jet are shown in the right hand panel of Figure 3. Also shown (as error bars) are the values of $a_{x,k}$ and $a_{y,k}$ corresponding to each peak, which give an estimate of the characteristic sizes (across and along the jet, respectively) of the observed structures.

In order to quantify the observed broadening of the jet, for each position y we compute the weighted mean of the x -spatial scale (perpendicular to the outflow axis):

$$\langle a_x \rangle = \frac{\sum_k a_{x,k} T_{a_{x,k}, a_{y,k}}(x_k, y)}{\sum_k T_{a_{x,k}, a_{y,k}}(x_k, y)}, \quad (3)$$

Figure 4 shows $\langle a_x \rangle$ as a function of position y along the HH 110 flow. In this figure, $y = 0$ corresponds to the position of the peak of knot A, and y grows moving South along the HH 110 axis. From knot A to the middle of knot C ($y = 0 \rightarrow 20''$), $\langle a_x \rangle$ grows from $\sim 3''$ to $\sim 7''$. For $y = 20'' \rightarrow 70''$, $\langle a_x \rangle$ increases more or less monotonically from $\sim 7''$ to $\sim 15''$. For $y = 70'' \rightarrow 90''$, $\langle a_x \rangle$ shows a more or less constant value with a small dispersion (with $\langle a_x \rangle$ values ranging from $\sim 10''$ to $\sim 13''$). For $y > 90''$, $\langle a_x \rangle$ shows a wide dispersion, with values ranging from $\sim 1''$ up to $\sim 15''$.

If we draw a straight line in Figure 4, passing through the peak $\langle a_x \rangle$ of knots A and L, we see that it forms an upper envelope to all of the values of $\langle a_x \rangle$ in this region (which includes all knots from A to L). From this upper envelope, we deduce that the emitting region (from $y = 0'' \rightarrow 70''$) broadens with a half-opening angle of 10°.

Finally, in Figure 5 we show the $a_{y,k}$ as a function of $a_{x,k}$ for different regions along the HH 110 jet. We plotted together the points with values of y in five different intervals along the jet beam (knots A-H, I-N, O-Q, R₁-R₂ and S, corresponding to the y -intervals given in Table 2). We find that for knots A-H, the $a_{y,k}$ (i. e., the spatial scales along the outflow axis) range from 1 to 18'', while the $a_{x,k}$ (i. e., the spatial scales across the outflow axis) have values of up to 15''.

For knots I-N, the $a_{x,k}$ values are either smaller than 6'' or larger than 12''. Interestingly, the intermediate scales, which are detected in other regions of the jet, do not appear as local maxima in the wavelet spectrum, and are therefore not picked up by the analysis described in §4.1.

While basically no correlation is seen between the $a_{y,k}$ and $a_{x,k}$ values in knots A-N, at larger distances from the source, these values appear to be correlated. For knots O-Q, the points more or less fall on a $a_{y,k}/a_{x,k} = 1.3$ line, even though there is a wide scatter for $a_{x,k} < 6''$. For knots R₁-R₂, the points roughly fall on $a_{y,k}/a_{x,k} = 0.5$ line, with the exception of few points which show large scales along and across the beam of the jet. Therefore, we see a transition from structures that are elongated along the outflow axis (for knots O-Q) to transversally oriented structures (for knots R₁-R₂). There are, however, some elongated structures at knots O-Q, and some large structures both across and along the beam of the jet at the location of knots R₁-R₂ (see Fig. 5). Finally, for the S-shaped structure (at $y > 140''$, which we have labeled S) both axially elongated and transversal structures appear to be present.

5. The spatial distributions of the radial velocities and the line widths

In order to describe the spatial dependence of the kinematical properties of the HH 110 flow, we compute two different moments of the line profiles:

$$V_c = \frac{\int v I_v dv}{\int I_v dv}, \quad (4)$$

$$W^2 = \frac{\int (v - V_c)^2 I_v dv}{\int I_v dv}, \quad (5)$$

for each spatial pixel of the position-velocity cube. In these equations, v is the radial velocity, and I_v the intensity (at a fixed position x, y) of the successive channel maps. We carry out the integrals over the radial velocity v_r by replacing them with sums over the velocity channel maps. V_c (see equation 4) is the barycenter of the line profile (which from now we will call the “line center” radial velocity), and W (equation 5) is a second order moment that reflects the width of the line profile.

We find that the value of W is quite strongly affected by the H II region (which is particularly bright in the surroundings of the faint S region, see figure 2). Therefore, we have subtracted this emission by fitting a linear dependence between the fluxes (seen in each channel map) in two rectangular regions (with a $10''$ width) on each side of the HH 110 jet.

With the values of V_c and W computed for all positions (x, y) on the plane of the sky, we then compute the following spatial averages:

$$\langle W^2 \rangle = \frac{\int_{S_{a_x, a_y}} W^2(x', y') I(x', y') dx' dy'}{\int_{S_{a_x, a_y}} I(x', y') dx' dy'}, \quad (6)$$

$$\langle V_c \rangle = \frac{\int_{S_{a_x, a_y}} V_c(x', y') I(x', y') dx' dy'}{\int_{S_{a_x, a_y}} I(x', y') dx' dy'}, \quad (7)$$

$$\langle \Delta v^2 \rangle = \frac{\int_{S_{a_x, a_y}} [V_c(x', y') - \langle V_c \rangle(x, y)]^2 I(x', y') dx' dy'}{\int_{S_{a_x, a_y}} I(x', y') dx' dy'}, \quad (8)$$

where $I(x', y')$ is the H α flux obtained from co-adding all of the channel maps. These integrals are carried out over areas S_{a_x, a_y} which are ellipses with central positions (x, y) and major/minor axes a_x and a_y corresponding to all of the wavelets that have been identified as peaks of the wavelet spectrum (see §4.1 and figure 3). $\langle W^2 \rangle^{1/2}(x, y)$ corresponds to the line width spatially averaged over the ellipse S_{a_x, a_y} with a weight $I(x', y')$ (see equation 6). We then compute the average of the line center velocities $\langle V_c \rangle$ within the ellipse, as well as the standard deviation $\langle \Delta v^2 \rangle^{1/2}$ of these velocities (see equations 7 and 8). Such deviations of the line center velocity, averaged over sizes chosen from a wavelet spectrum, have been previously used by Gill & Henriksen (1990) to study turbulence in molecular clouds.

We then obtain values for $\langle W^2 \rangle^{1/2}$, $\langle V_c \rangle$ and $\langle \Delta v^2 \rangle^{1/2}$ at all of the central points of the wavelets shown in Figure 3 (corresponding to peaks in the wavelet spectrum). In Figure 6, we show the line centers, widths and standard deviations as a function of position y along the jet (all of the points at different positions x across the jet beam and with different a_x and a_y are plotted).

$\langle V_c \rangle$ as a function of position y shows quite a wide scatter, and a general trend of more negative velocities from knot A ($\langle V_c \rangle \sim -5$ km s $^{-1}$) to knots P-Q ($\langle V_c \rangle \sim -35$ km s $^{-1}$). If we measure these radial velocities with respect to the surrounding molecular cloud (with a heliocentric radial velocity of +23 km s $^{-1}$, see Reipurth & Olberg 1991) and correct for an orientation angle of 35° with respect to the plane of the sky (Riera et al. 2003), we then obtain that the (de-projected) jet velocity grows from ~ 50 to ~ 100 km s $^{-1}$ from knot A out to knots P-Q. This is in good agreement with the results obtained from long-slit spectra by Riera et al. (2003).

At larger distances ($y > 120''$), $\langle V_c \rangle$ grows, reaching ≈ 0 at $y = 145''$, and then remaining with slightly negative values up to the end of the detected emission. We believe that this behaviour of $\langle V_c \rangle$ for $y > 120''$ could be a result of changes in the orientation angle of the outflow with respect to the plane of the sky (because in this region, substantial side-to-side excursions of the jet beam are observed on the plane of the sky, see Figure 3), and might therefore not reflect a real slowing down of the jet flow.

The standard deviation $\langle \Delta v^2 \rangle^{1/2}$ of the line center velocity (see Figure 6) appears not to have any dependence on position y along the jet beam (showing values mostly within

the 7 to 15 km s⁻¹ range) out to knot M ($y \sim 75''$). Beyond knot N ($y > 90''$), $\langle \Delta v^2 \rangle^{1/2}$ shows a more or less monotonic growth, reaching a value of ~ 25 km s⁻¹ at $y = 175''$.

The average line widths $\langle W^2 \rangle^{1/2}$ do not show a systematic trend with position along the jet, mostly staying within a range from 35 to 45 km s⁻¹. This width of course includes the instrumental profile, which has a value of ≈ 32 km s⁻¹.

An interesting feature is that many of the points in the $\langle V_c \rangle$, $\langle \Delta v^2 \rangle^{1/2}$ and $\langle W^2 \rangle^{1/2}$ vs. y plots (see figure 3) appear to fall on more or less monotonic curves. This is somewhat surprising given the complex structure of the HH 110 outflow. As might be expected, the points which fall on the monotonic curves are the spatial averages corresponding to the wavelets with larger sizes ($a_x, a_y \sim 10''$, see figures 4 and 5), which naturally give a smoother dependence of the average quantities as a function of position along the jet.

The fact that the averages over sizes of $\sim 10''$ give smooth curves as a function of position indicates that the kinematical properties of the flow have structures only in sizes $< 10''$, which are superimposed on a smooth dependence on position along the jet axis. To some extent, this result is a quantification of the fact that while the H α intensity map of HH 110 has complex, high contrast structures with many different spatial scales, the radial velocity and line width maps of this object only show small scale structures which are superimposed on a generally smooth distribution as a function of position along the jet (see figure 2).

In Figure 7, we plot the line centers, widths and standard deviations as a function of position x across the jet (all of the points with different a_x and a_y are plotted). We plotted together the points with values of y in five different intervals along the jet beam (given in Table 2).

$\langle V_c \rangle$ shows basically flat structures as a function of x (i. e., across the jet beam) in the regions of knots A to N. For the three regions at larger distances from the source (O-Q, R₁-R₂ and S), either growing or decreasing $\langle V_c \rangle$ vs. x trends are seen. The average line width $\langle W^2 \rangle^{1/2}$ shows basically no trend as a function of x .

For knots A-N, the dispersion of the line center $\langle \Delta v^2 \rangle^{1/2}$ shows a central region (with $|x| < 6''$) with values ranging from zero to 12 km s⁻¹, and two outer peaks (with $|x| = 6 \rightarrow 10''$) with larger velocity dispersions of up to ~ 20 km s⁻¹. The central, low velocity dispersion region therefore has a diameter of $\sim 12''$ (8×10^{16} cm at 460 pc), and is surrounded by a high velocity dispersion envelope with an outer diameter of $\sim 16''$ (1.1×10^{17} cm).

Finally, in Figure 8 we show the values of $\langle \Delta v^2 \rangle^{1/2}$ and $\langle W^2 \rangle^{1/2}$ as a function of

the size a_x (across the jet beam) of the ellipses over which the averages have been computed. Again, we divide the points into the five chosen regions along the outflow axis.

From Figure 8, it is clear that both $\langle \Delta v^2 \rangle^{1/2}$ and $\langle W^2 \rangle^{1/2}$ show very clear trends as a function of the size scale a_x . The $\langle W^2 \rangle^{1/2}$ values are approximately constant as a function of a_x , and show a decreasing scatter for larger a_x . The $\langle \Delta v^2 \rangle^{1/2}$ values also show a decreasing scatter as a function of a_x , but this decrease in scatter is superimposed on a shallow trend of increasing $\langle \Delta v^2 \rangle^{1/2}$ vs. a_x .

Interestingly, in this representation (of $\langle \Delta v^2 \rangle^{1/2}$ and $\langle W^2 \rangle^{1/2}$ vs. a_x), the line widths and central velocity variations show a quite systematic behaviour. Because of this, we choose this particular representation in order to try to interpret the kinematical characteristics of the HH 110 jet. This is done in the following section.

6. A turbulent wake (or jet) model

It is not immediately clear what the observed line widths and radial velocity dispersions as a function of spatial scale are actually telling us. In order to interpret these results, we use a simple, analytic model (described in Cantó, Raga & Riera 2003), which allows at least a partial understanding of the implications of the observations. This model is as follows.

It is known from laboratory experiments that the mean flow velocity of a turbulent jet or wake has a centrally peaked cross section. Superimposed on this flow are the turbulent fluctuations, which cannot be modeled in detail.

HH 110 has a complex structure, probably formed by irregularly shaped shocks which give rise to the observed emission line knots. The observed spatially resolved line profiles are then the result of a mean motion along the jet flow (the “mean flow”) combined with the scattered motions resulting from the non-planar shocks (the “turbulent velocities”, in analogy to the standard description of a laboratory jet). The distribution of the radial velocity (projected along the line of sight) over the cross section of the jet will then be determined by the appropriately projected distributions of the mean and turbulent velocities.

As a simple parametrization of the mean flow velocity, we assume that it is directed along the outflow axis, and that it has a dependence on the cylindrical radius r which is given by a generic Taylor series expansion of the form $v_j = a + br + cr^2 + \dots$. One can argue that the first order term should be null, since it leads to an unphysical on-axis “cusp” in the distribution. Therefore, the lowest order function that we can consider is quadratic. We will

then assume that the radial velocity cross section of the jet is given by

$$v_j(r) = v_0 \left(1 - \frac{r^2}{h^2} \right), \quad (9)$$

where v_0 is the central velocity and h the outer radius of the jet beam. It is assumed that both v_0 and h vary along the jet beam only in scales much larger than the jet width.

If the jet axis lies at an angle ϕ with respect to the plane of the sky (moving away from the observer), the profile of an emission line for a point within the jet is given by :

$$j_v = \frac{j_0}{\sqrt{\pi} \Delta v_T} e^{-[(v-v_r)/\Delta v_T]^2}, \quad (10)$$

where

$$v_r = v_0 \sin \phi \left[1 - \frac{x^2 + z^2 \cos^2 \phi}{h^2} \right]. \quad (11)$$

In this equation, x is measured across the section of the jet, and z along the line of sight (with $x, z = 0, 0$ on the outflow axis). The line width Δv_T includes both the thermal width and the turbulent velocity (the instrumental width could be added as well to this term in order to reproduce observed results), and is assumed to be independent of position within the jet. We also assume that the emitted energy per unit time, volume and solid angle in the line j_0 is independent of position (see Cantó, Raga & Riera 2003).

The line intensity at a distance x from the jet axis will then be

$$I_v(x) = 2 \int_0^{z_m} j_v dz, \quad (12)$$

where

$$z_m = \frac{(h^2 - x^2)^{1/2}}{\cos \phi}. \quad (13)$$

One can then compute the barycenter velocity

$$V_c(x) = \frac{2}{3} v_0 \sin \phi \left(1 - \frac{x^2}{h^2} \right), \quad (14)$$

and the line width

$$W^2(x) = \frac{\Delta v_T^2}{2} + \frac{4}{45} v_0^2 \sin^2 \phi \left(1 - \frac{x^2}{h^2} \right)^2, \quad (15)$$

by carrying out the integrals of equations (4) and (5).

Now, from our Fabry-Pérot observations we have computed averages of the line width over regions of different characteristic sizes a across the width of the jet. In our model, this can be computed as

$$\langle W^2 \rangle (a, x) = \frac{1}{2a} \int_{x-a}^{x+a} w^2(x') dx' = \frac{\Delta v_T^2}{2} + \frac{4}{45} v_0^2 \sin^2 \phi \left[\frac{1}{5} \frac{a^4}{h^4} - \frac{2}{3} \frac{a^2}{h^2} \left(1 - 3 \frac{x^2}{h^2} \right) + \left(1 - \frac{x^2}{h^2} \right)^2 \right]. \quad (16)$$

We can also compute the spatially averaged line center velocity

$$\langle V_c \rangle (a, x) = \frac{1}{2a} \int_{x-a}^{x+a} V_c(x') dx' = \frac{2}{3} v_0 \sin \phi \left[1 - \frac{x^2}{h^2} - \frac{a^2}{3h^2} \right], \quad (17)$$

as well as the square of the standard deviation of the line center velocities

$$\langle \Delta v^2 \rangle (a, x) = \frac{1}{2a} \int_{x-a}^{x+a} [V_c(x') - \langle V_c \rangle (a, x)]^2 dx' = \frac{16}{27} v_0^2 \sin^2 \phi \left(\frac{a}{h} \right)^2 \left[\frac{x^2}{h^2} + \frac{a^2}{15h^2} \right]. \quad (18)$$

Equations (16) and (18) define an upper envelope and a lower envelope for the possible values that $\langle W^2 \rangle$ and $\langle \Delta v^2 \rangle$ can take as a function of the averaging scale a . These envelopes are obtained by setting $x = 0$ (averaging interval centered on the jet axis), and $x = h - a$ (averaging interval touching the outer edge of the jet beam). Setting $x = 0$, we obtain a lower envelope for $\langle W^2 \rangle^{1/2}$ and an upper envelope for $\langle \Delta v^2 \rangle^{1/2}$:

$$\langle W^2 \rangle^{1/2}_{low}(a) = \left\{ \frac{\Delta v_T^2}{2} + \frac{4}{45} v_0^2 \sin^2 \phi \left[\frac{1}{5} \frac{a^4}{h^4} - \frac{2}{3} \frac{a^2}{h^2} + 1 \right] \right\}^{1/2}, \quad (19)$$

$$\langle \Delta v^2 \rangle^{1/2}_{up}(a) = \frac{4}{9\sqrt{5}} v_0 \sin \phi \left(\frac{a}{h} \right)^2. \quad (20)$$

Setting $x = h - a$, we obtain an upper envelope for $\langle W^2 \rangle^{1/2}$ and a lower envelope for $\langle \Delta v^2 \rangle^{1/2}$:

$$\langle W^2 \rangle^{1/2}_{up}(a) = \left\{ \frac{\Delta v_T^2}{2} + \frac{64}{45} v_0^2 \sin^2 \phi \left(\frac{a}{h} \right)^2 \left[\frac{1}{5} \frac{a^2}{h^2} - \frac{1}{2} \frac{a}{h} + \frac{1}{3} \right] \right\}^{1/2}, \quad (21)$$

$$\langle \Delta v^2 \rangle^{1/2}_{low}(a) = \frac{4}{9\sqrt{5}} v_0 \sin \phi \left(\frac{a}{h} \right) \left[\left(\frac{a}{h} \right)^2 + 15 \left(1 - \frac{a}{h} \right)^2 \right]^{1/2}. \quad (22)$$

The curves for $\langle W^2 \rangle^{1/2}_{low}$ and $\langle W^2 \rangle^{1/2}_{up}$ (as well as the ones for $\langle \Delta v^2 \rangle^{1/2}_{low}$ and $\langle \Delta v^2 \rangle^{1/2}_{up}$) meet at the maximum possible value for the averaging length a (i. e., at $a = h$).

We have drawn the curves given by equations (19-22) on the corresponding plots of Figure 8. For each section along the jet we have chosen values of h and $v_0 \sin \phi$ such that

for $a = h$ (when the upper and lower envelopes join, see above) the model coincides with the value of $\langle \Delta v^2 \rangle^{1/2}$ corresponding to the largest measured scale length perpendicular to the HH 110 axis, which has $a_x = a_{x,max}$ and $\langle \Delta v^2 \rangle^{1/2} = \langle \Delta v^2 \rangle_{max}^{1/2}$. In other words, we choose $h = a_{x,max}$ and $v_0 \sin \phi = (9/4)\sqrt{5}\langle \Delta v^2 \rangle_{max}^{1/2}$. We then choose a value for Δv_T so that for $a = h$ the model prediction coincides with the outer point of the observed $\langle W^2 \rangle^{1/2}$ vs. a points. The values of h , $v_0 \sin \phi$ and Δv_T resulting from these fits to the different regions along the HH 110 jet are given in Table 2.

Interestingly, we again find an acceleration along the HH 110 jet, with v_0 increasing from 113 km s⁻¹ (in the A-H region) to 200 km s⁻¹ (in the S region). We can use the obtained values of $v_0 \sin \phi$ to calculate the maximum on-axis value $\langle V_c \rangle_{max} = (2/3)v_0 \sin \phi$ (obtained by setting $x = 0$ and $a = 0$ in equation 17). The resulting values (which are also given in Table 2) should be compared with the observations by looking at the on-axis values of $\langle V_c \rangle_{axis}$ in Figure 7. From this figure, we obtain $\langle V_c \rangle_{axis} = -12, -15, -22, -18$ and -7 km s⁻¹ for the five chosen regions. If we consider the absolute values of the corresponding velocities with respect to the cloud (which has $V_{hel} = +23$ km s⁻¹), we obtain $|\langle V_c \rangle_{axis} - V_{hel}| = 35, 38, 45, 41$ and 30 km s⁻¹. For knots A-Q, these values lie within 20 % of the $\langle V_c \rangle_{max}$ values obtained from the fits to the $\langle \Delta v^2 \rangle^{1/2}$ plots (see figure 8 and table 2).

Also interesting is the fact that in order to fit the observed $\langle W^2 \rangle^{1/2}$ (a_x) values, we need to include a line broadening of $\Delta v_T \approx 45$ km s⁻¹. If we subtract in quadrature the 32 km s⁻¹ instrumental resolution, we obtain an intrinsic broadening $\Delta v_{T,int} = 35 \rightarrow 46$ km s⁻¹. These values are substantially larger than the ~ 10 km s⁻¹ expected thermal width, so that they therefore probably reflect turbulent motions in the jet flow.

Looking at Figure 8, we see that the observed $\langle W^2 \rangle^{1/2}$ and $\langle \Delta v^2 \rangle^{1/2}$ mostly lie on the model predictions for averaging intervals centered on the outflow axis (equations 19 and 20, respectively). This is not surprising since the wavelets chosen by our knot detection algorithm mostly lie close to the HH 110 axis (see figure 3).

However, for $a_x < 5''$ we see that the observed $\langle W^2 \rangle^{1/2}$ and $\langle \Delta v^2 \rangle^{1/2}$ values lie substantially above the theoretical curves. In particular, the points corresponding to regions that lie further away from the outflow axis (shown with open circles in figure 8) are the ones that tend to have larger velocity dispersions. These points can be clearly seen to lie in the outer, high velocity dispersion envelope which is seen in the cross sections shown in Figure 7 (also see section 5). We speculate that this envelope corresponds to a turbulent boundary layer (which is not present in our simple, analytic jet model) with higher turbulent velocities than the central region of the jet beam.

7. Conclusions

We have obtained a Fabry-Pérot position-velocity H α cube of the HH 110 flow. Both the velocity channel maps and the integrated H α image show a complex structure of knots distributed in a broadening, more or less conical structure.

Given the description-defying complexity of the structure, we have chosen to carry out an anisotropic wavelet analysis of the H α image, which automatically detects the position and characteristic sizes (along and across the jet axis) of the knots. From this analysis, we find that the jet first opens out in a cone with a half-opening angle of $\sim 10^\circ$ for distances up to $70''$ from knot A, and has a constant width out to knot R.

We have then computed the central velocity, the velocity width and the dispersion of the central velocity of the line profiles, averaged over ellipses corresponding to the sizes of the structures detected by the wavelet analysis. These quantities show that while there is an acceleration of the jet out from knot A to knot Q (in the region within $120''$ from knot A), the line width and central velocity dispersion remain relatively constant. A more complex behaviour is seen for knots R-S, which could be a reflection of the fact that in this region the jet has a curved structure (in the plane of the sky, and therefore probably also along the line of sight).

Across the beam of the jet, we see that there is a central, low velocity dispersion region with a diameter of $\sim 12''$, surrounded by a higher velocity dispersion envelope with an outer diameter of $\sim 16''$. This result could be evidence for the existence of a turbulent boundary layer in the outer regions of the HH 110 jet beam.

Finally, for 5 different regions along the jet beam, we have plotted the mean velocity width $\langle W^2 \rangle^{1/2}$ and central velocity dispersion $\langle \Delta v^2 \rangle^{1/2}$ as a function of the size scale a_x (perpendicular to the jet axis) of the detected structures. We find that these plots show well organized behaviours.

Interestingly, we find that it is possible to model the observed $\langle W^2 \rangle^{1/2}(a_x)$ and $\langle \Delta v^2 \rangle^{1/2}(a_x)$ profiles with a simple, analytic model of a turbulent jet (or wake). From a comparison of the models with the data, we deduce that most of the observed values can be explained with a model with an axially peaked mean flow velocity, with superimposed turbulent (+thermal) motions with a velocity dispersion of $\sim 40 \text{ km s}^{-1}$.

However, for characteristic sizes $< 5''$, the observed velocity dispersions lie up to $\sim 25 \text{ km s}^{-1}$ above the model prediction. We find that these points correspond to the outer, high velocity dispersion envelope of the HH 110 jet (see above). Therefore, in this representation we again see the presence of what appears to be a turbulent boundary layer, which is not

present in our analytic turbulent jet/wake model.

Finally, we should note that the acceleration observed along the HH 110 jet does not agree with what one would expect for a turbulent jet. A turbulent jet incorporates low momentum material from the surrounding environment, which leads to a progressive decrease of the flow velocity as one moves downstream along the jet beam (see, e. g., Raga et al. 1993). Therefore, the acceleration observed along the HH 110 jet would favour an interpretation of this flow in terms of a turbulent wake, rather than a jet. This is the scenario proposed by Raga et al. (1993), who modeled HH 110 in terms of a wake left behind by a jet deflected by the surface of a dense cloud, and then pinched off as the incident jet starts to burrow into the cloud.

Of course, another possibility would be to have a turbulent jet ejected with a monotonically increasing initial velocity. If this increase in the ejection velocity were drastic enough, it could overcome the drag due to the entrainment of environmental material, and lead to an “acceleration” down the jet axis similar to the one observed in HH 110.

To conclude, we would like to point out that this work represents a first attempt to apply wavelet analysis techniques to observations of astrophysical jets. A spectrum of a 2D image with anisotropic wavelet basis functions is defined in a four-dimensional space (with two spatial and two spectral dimensions), and therefore contains a large amount of information which is difficult to interpret. The present analysis is based only on a study of the spatial and spectral maxima of the wavelet spectrum (i. e., on finding “knots” and their characteristic sizes), and clearly does not use a lot of the information present in the wavelet spectrum.

The work of A. Raga and JC was supported by the CONACyT grant 36572-E and 34566-E. A. Riera acknowledges the ICN-UNAM for support during her sabbatical. The work of A. Riera was supported by the MCyT grant AYA2002-00205 (Spain). BR acknowledges support for this project from NASA grant NAG5-8108 (LTSA) and NSF grant AST-9819820. We acknowledge Lucila González for her help with the manuscript.

REFERENCES

- Amram P., Balkowski C., Boulesteix J., Cayatte V., Marcelin M. & Sullivan W., 1996, *A&A*, 310, 737
- Amram P., Boulesteix, J., Marcelin, M., Balkowski, C., Cayatte, V. & Sullivan, W.T., III, 1995, *A&As*, 113, 35
- Amram, P., Le, Coarer, E., Marcelin, M., Balkowski, C., Sullivan, W. T. III & Cayatte, V. 1992, *A&As*, 94, 175
- Amram, P., Marcelin, M., Balkowski, C., Cayatte, V., Sullivan, W. T. III & Le Coarer, E. 1994, *A&As*, 103, 5
- Amram, P., Mendes de Oliveira, C., Boulesteix, J. & Balkowski, C., 1998, *A&A*, 330, 881
- Amram, P., Sullivan, W., Balkowski, C., Marcelin, M. & Cayatte, V., 1993, *ApJ*, 403, L59
- Bendjoya, Ph., Slézak, E. & Froeschlé, Cl., 1991, *A&A*, 251, 312
- Cantó, J., Raga, A.C. & Riera, A. 2003, *RMxAA* (submitted)
- Choi, M., 2001, *ApJ*, 550, 817
- Davis, C. J., Mundt, R. & Eislöffel, J., 1994, *ApJ*, 437, L55
- Gill, A. G. & Henriksen, R. N., 1990, *ApJ*, 365, L27
- de Gouveia Dal Pino, E. M., 1999, *ApJ*, 526, 862
- Holschneider, M. 1995, *Wavelets : an analysis tool*, Oxford University
- Hurka, J. D., Schmid-Burgk, J. & Hardee, P. E., 1999, *A&A*, 343, 558
- Laval, A., Boulesteix, J., Georgelin, Y. P., Georgelin, Y. M. & Marcelin, M. 1987, *A&A*, 175, 199
- Noriega-Crespo, A., Garnavich, P. M., Raga, A. C., Cantó, J. & Böhm, K. H., 1996, *ApJ*, 462, 804
- Raga, A. C., Cantó, J., 1995, *RMxAA*, 31, 51
- Raga, A. C., Cantó, J., Calvet, N., Rodríguez, L. F. & Torrelles, J. M., 1993, *A&A*, 276, 539
- Raga, A. C., de Gouveia Dal Pino, E. M., Noriega-Crespo, A., Mininni, P. D. & Velázquez, P. F., 2002, *A&A*, 392, 267

Raga, A. C., Mundt, R. & Ray, T. P., 1991, *A&A*, 246, 535

Reipurth, B. & Olberg, M., 1991, *A&A*, 246, 535

Reipurth, B., Raga, A. C. & Heathcote, S., 1996, *A&A*, 311, 989

Riera, A., López, R., Raga, A. C., Estalella, R. & Anglada, G., 2003, *A&A*, 400, 213

Rodríguez, L. F., Reipurth, B., Raga, A. C. & Cantó, J., 1998, *RMxAA*, 34, 69

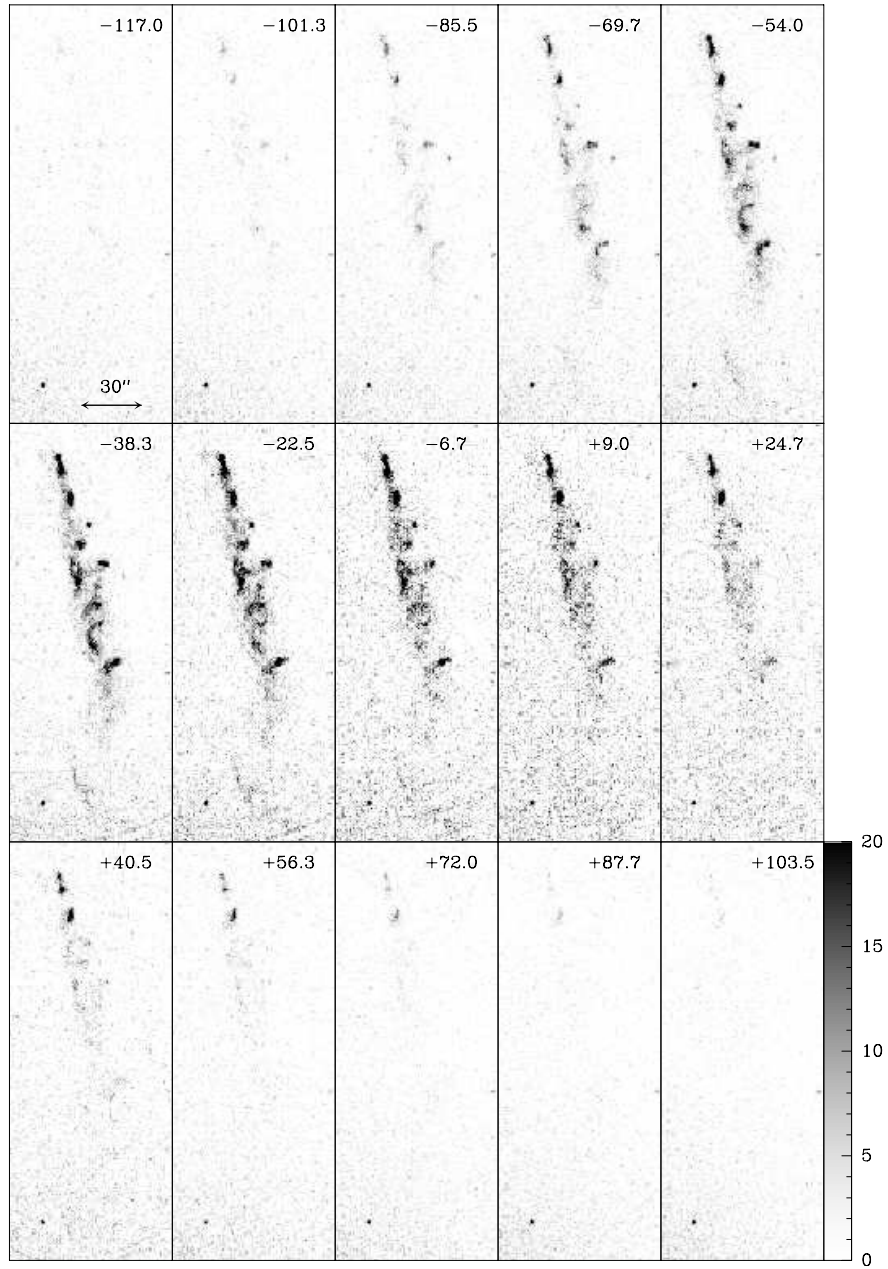


Fig. 1.— H α velocity channel maps corresponding to various radial velocities obtained from the Fabry-Pérot data of HH 110. The heliocentric radial velocities are indicated. The systemic velocity of the ambient cloud is +23 km s⁻¹. The scale (in arcsec) is given in the top left hand plot. The maps are shown with a linear greyscale given (in counts) by the bar.

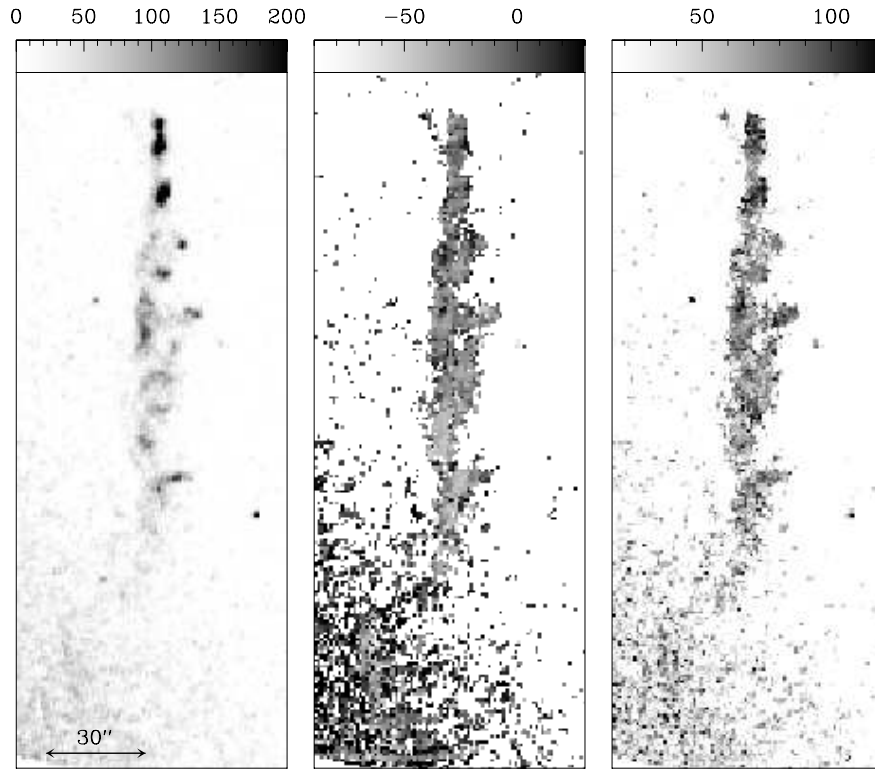


Fig. 2.— The H α image map (left panel), central radial velocity map (central panel) and the line widths (FWHM, right panel) obtained from the position-velocity cube. We have rotated the maps by 13° so that the outflow is more or less parallel to the y -axis. The greyscales of the map (linear, in counts) and of the central radial velocity and line width (linear, in km s^{-1}) are given by the bars on top of each plot.

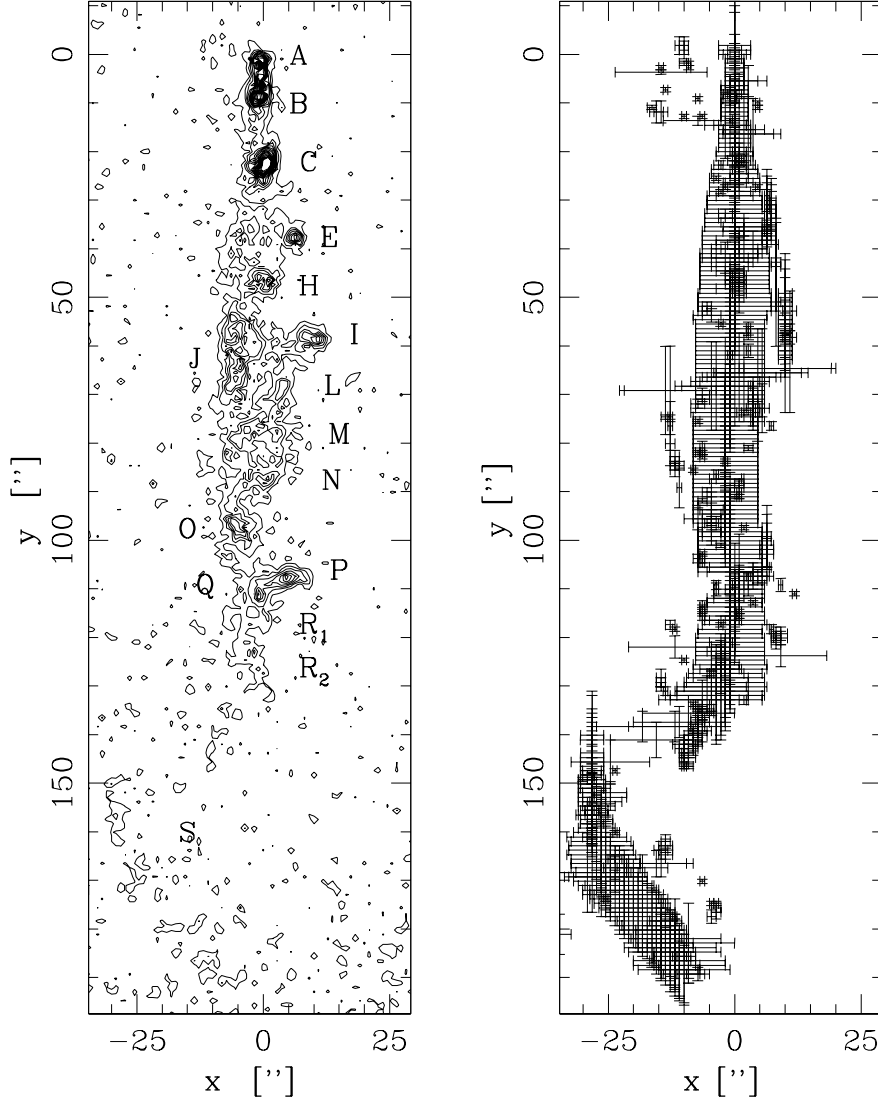


Fig. 3.— Left panel: contour plot of the H α image, where we have labelled the knots to help with their identification. Right panel: the positions and characteristic sizes of the structures along the HH 110 jet. The crosses show the positions of the maxima x_k of the wavelet transform obtained for the different values y along the jet. The characteristic sizes $a_{x,k}$ and $a_{y,k}$ of these maxima are shown as error bars centered on the positions of the maxima. The distances x (across the jet axis) and y (along the jet axis) are measured from the peak of knot A. We have rotated the maps by 13° so that the outflow is more or less parallel to the y -axis.

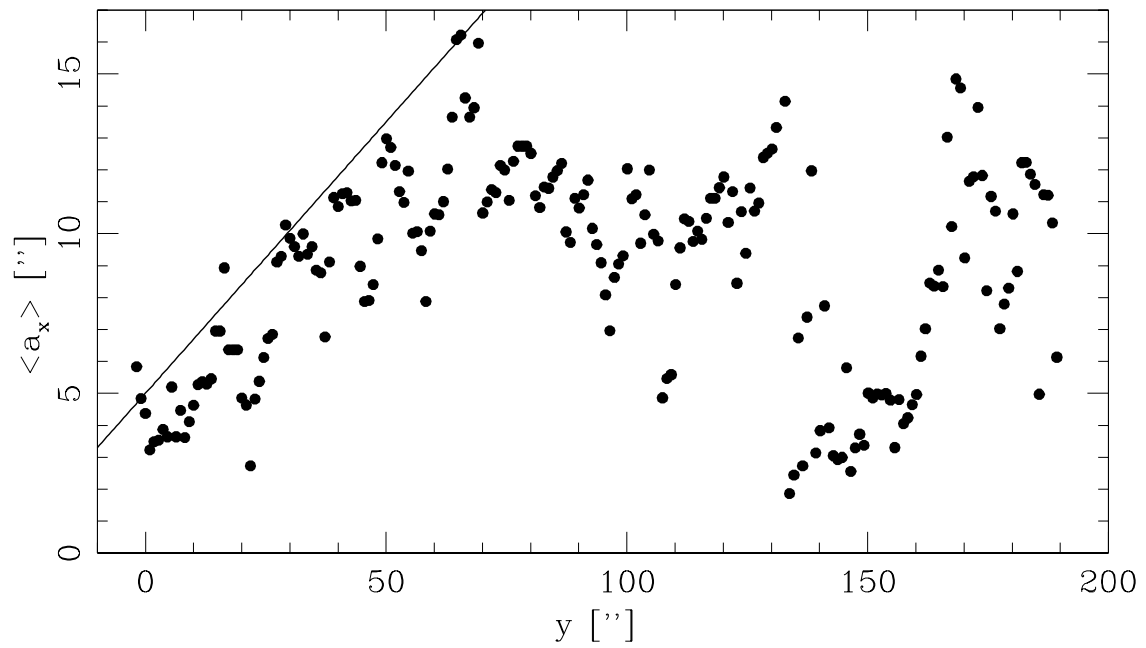


Fig. 4.— The $\langle a_x \rangle$ are plotted as a function of position y along the HH 110 jet. A straight line that forms an upper envelope to the $\langle a_x \rangle$ values (in the $y < 70''$ region) has been drawn (see the text).

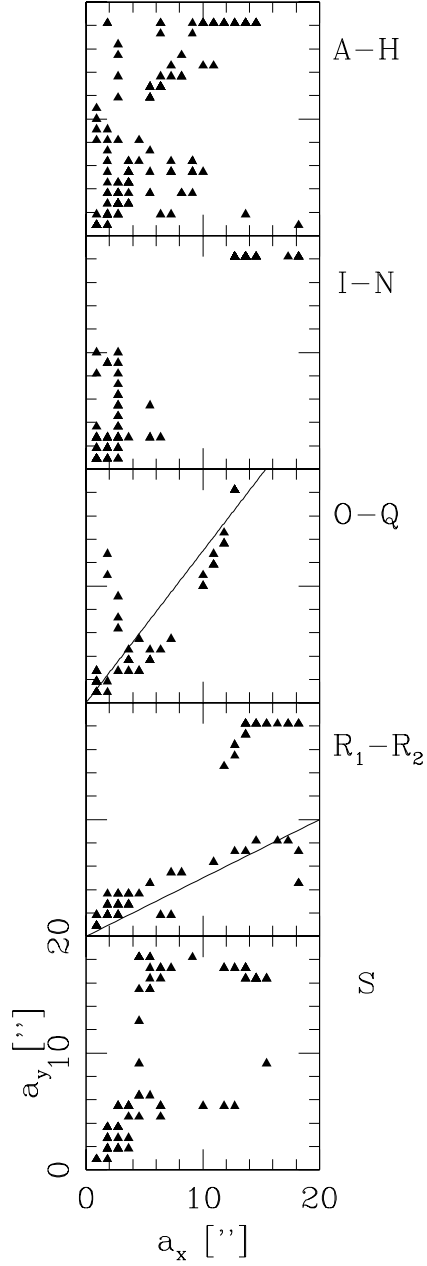


Fig. 5.— The $a_{y,k}$ are plotted as a function of $a_{x,k}$ for different regions along the HH 110 flow (see Table 2). For regions O-Q and R_1-R_2 the results from linear fits to the points are drawn as solid lines.

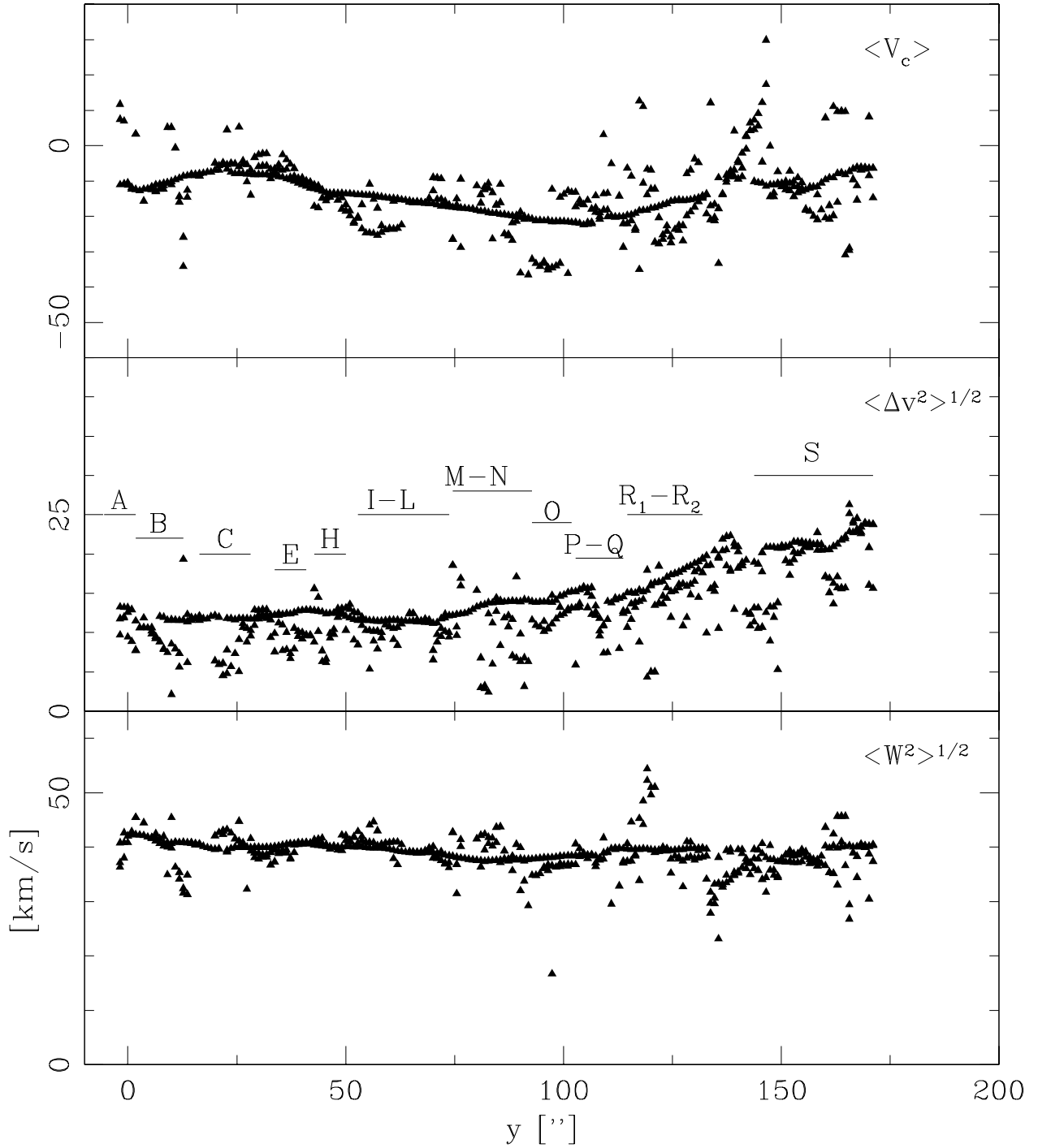


Fig. 6.— The average line centers (top panel), line widths (central panel) and standard deviations (bottom panel) as a function of position y along the HH 110 jet. All points with different positions x across the jet and with different a_x and a_y are plotted.

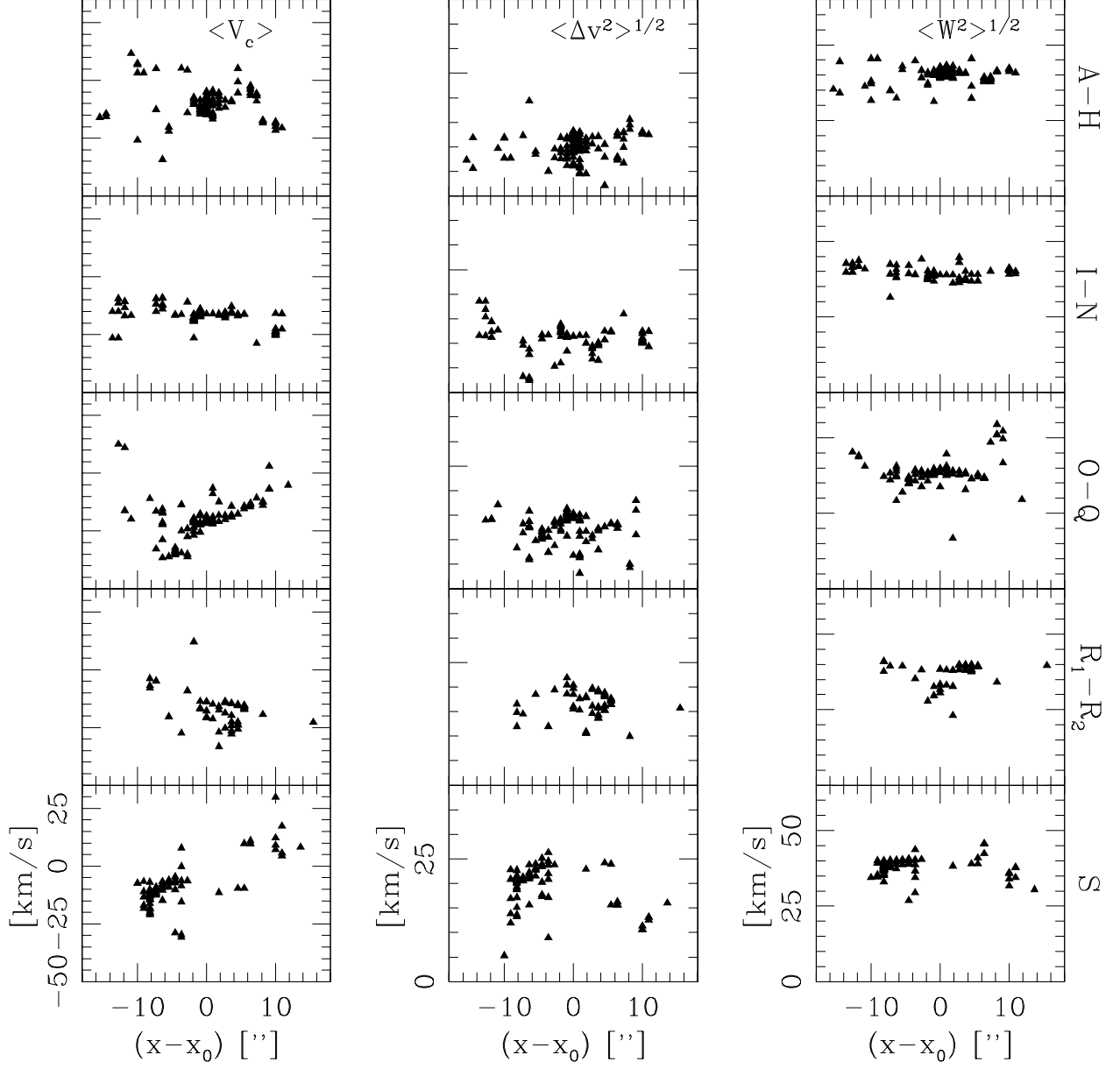


Fig. 7.— The line centers (left), line widths (center) and standard deviations (right) are plotted as a function of position x across the jet beam for the 5 different chosen regions along the HH 110 flow. x_0 is the central position of the jet cross section (which varies along the jet, as the beam has side-to-side excursions, see figure 3).

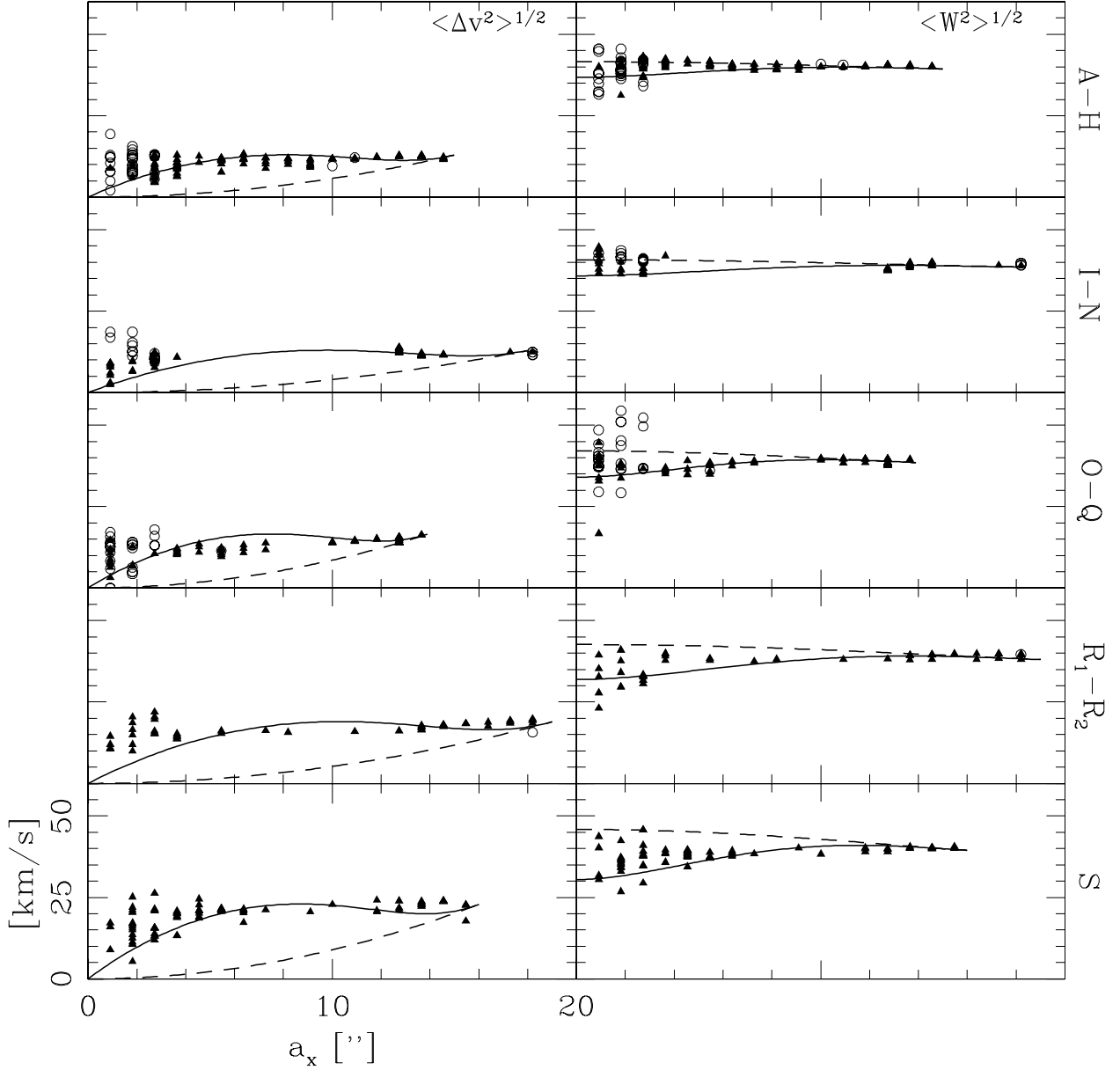


Fig. 8.— The average standard deviations of the line center (left panels) and the line widths (right panels) obtained from the data cube are plotted as a function of the size scale $\langle a_x \rangle$ across the jet flow for the 5 chosen regions along the jet. The triangles correspond to points which lie in the central region of the flow (with $|x| \leq 3''$ for the A-H region, $|x| \leq 7''$ for the I-N region, $|x| \leq 5''.5$ for the O-Q region, and $|x| \leq 9''$ for the R₁-R₂ region), and the open dots correspond to the outer region of the jet beam (see section 6). The curves correspond to the predictions of the analytical model, which have been fitted independently for each region along the HH 110 jet (see section 6). In the left panels, the curves correspond to $\langle \Delta v^2 \rangle_{up}^{1/2}$ (solid line) and $\langle \Delta v^2 \rangle_{low}^{1/2}$ (dashed line). In the right panels, the curves correspond to $\langle W^2 \rangle_{up}^{1/2}$ (solid line) and $\langle W^2 \rangle_{low}^{1/2}$ (dashed line).

Table 1. Journal of Fabry-Pérot observations

Observations	Telescope	ESO 3.6m
	Equipment	CIGALE @ Cassegrain
	Date	1997, January, 4-6
	Seeing	0''4 → 0''8
Calibration	Neon Comparison light	λ 6598.95 Å
Fabry-Pérot	Interference Order	793 @ 6562.78 Å
	Free Spectral Range at H α	380 km s ⁻¹
	<i>Finesse</i> ^a at H α	11
	Spectral resolution at H α	9400 ^b
Sampling	Number of Scanning Steps	24
	Sampling Step	0.35 Å (16 km s ⁻¹)
	Total Field	170'' × 170'' (256 × 256 px ²)
	Pixel Size	0.91''
Detector		IPCS (Thomson tube)

^aMean Finesse through the field of view

^bFor a signal to noise ratio of 5 at the sample step

Table 2. Model fits to the HH 110 jet

Region	y_{min}, y_{max} [']	h [']	$v_0 \sin \phi$	v_0	$\langle V_c \rangle_{max}$ [km s ⁻¹]	Δv_T	$\Delta v_{T,int}$
A-H	-11, 53	15	65	113	43	52	46
I-N	53, 85	18	65	113	43	51	45
O-Q	85, 121	14	83	145	55	48	41
R ₁ -R ₂	121, 136	19	95	166	63	45	37
S	144, 171	16	115	200	77	43	35

Note. — y_{min}, y_{max} give the position of the chosen regions along the HH 110 jet, where $y = 0$ corresponds to the peak of knot A. h is the outer radius of the jet beam and $v_0 \sin \phi$ is the central radial velocity of the model fit to the data (see section 6). The deprojected velocity v_0 was computed assuming an inclination angle $\phi = 35^\circ$ with respect to the plane of the sky. $\langle V_c \rangle_{max}$ is the maximum on axis value for the barycenter of the line profile computed from the model fit. Δv_T is the turbulent+thermal+instrumental line width necessary to fit the observed $\langle W^2 \rangle^{1/2}$ vs. a (see section 6). $\Delta v_{T,int}$ is the intrinsic broadening, computed subtracting in quadrature the instrumental width from Δv_T , where $\Delta v_{ins} = (FWHM_{ins})/(2(\ln 2)^{1/2})$. For an instrumental $FWHM = 34$ km s⁻¹, a $\Delta v_{ins} = 25$ km s⁻¹ is obtained.